Supplementary Material

Significantly improved conductivity of spinel Co_3O_4 porous nanowires partially substituted by Sn in tetrahedral sites for high-performance quasi-solid-state supercapacitors

Yunjian Chen,[a] Jia Zhu,[b,*] Ni Wang,[a,c] Huanyu Cheng,[b] Xianzhong Tang,[a] Sridhar Komarneni,[c,*] Wencheng Hu[a,*]

[a] School of Materials and Energy, University of Electronic Science & Technology of China, Chengdu 611731, P. R. China

[b] Department of Engineering Science and Mechanics, The Pennsylvania State University, University Park, Pennsylvania 16802, USA

[c] Materials Research Institute and Department of Ecosystem Science and Management, 204 Energy and Environment Laboratory, The Pennsylvania State University, PA, 16802, USA

*Corresponding Authors: J. Zhu (jmz5364@psu.edu), S. Komarneni (sxk7@psu.edu), W. Hu (huwc@uestc.edu.cn)

1. Materials

Cobalt acetate tetrahydrate ($Co(Ac)_2 \cdot 4H_2O$, AR, CAS: 71-48-7), stannous chloride dihydrate ($SnCl_2 \cdot 2H_2O$, AR, CAS: 10025-69-1), ammonium fluoride (NH_4F, AR, CAS:12125-01-8), polyethylene glycol (PEG 200, AR, CAS: 25322-68-3), ferrous sulfate ($FeSO_4 \cdot 7H_2O$, AR, CAS: 7720-78-7), aqueous ammonia ($NH_3 \cdot H_2O$, 25%, CAS: 1336-21-6), Poly(vinyl alcohol) 1799 (PVA 1799, AR, CAS: 9002-89-5), and potassium hydroxide (KOH, AR, CAS: 1310-58-3) were obtained from Aladdin Ltd. (Shanghai, China). All the reagents were used as received without further purification.

2. The calculation of electrochemical performance

Based on the GCD curves, the specific capacity (C, F g^{-1}) of the electrodes in a three-electrode system can be calculated according to the equation (S1):

$$C = \frac{i \times \Delta t}{m \times \Delta U} \tag{S1}$$

where i (A) is the applied current, Δt (s) is the discharge time, m (g) is the mass of the electroactive materials in the electrodes, and ΔU (V) is the potential window in the discharging process.

In a two-electrode system, the specific capacitance (C, F g^{-1}) can be calculated from GCD curves according to the equation (S2):

$$C = \frac{i \times \Delta t}{m \times \Delta U} \tag{S2}$$

where i (A) represents the discharge current, m (g) is the mass of the whole electroactive materials in the ASC device, Δt (s) is the discharge time, ΔU (V) is the potential window in the discharging process.

For the ASC device, energy density (E, Wh kg^{-1}) and power density (P, W kg^{-1}) were calculated using the equation (S3) and (S4), respectively.

$$E = \frac{C \times \Delta U^2}{7.2} \tag{S3}$$

$$P = \frac{3600 \times E}{\Delta t} \tag{S4}$$

where C (F g^{-1}) is the volumetric capacitance (F g^{-1}), ΔU (V) is the potential window in the discharging process, and Δt (s) is the discharge time from GCD curves.

3. The cross-sectional SEM image of GF

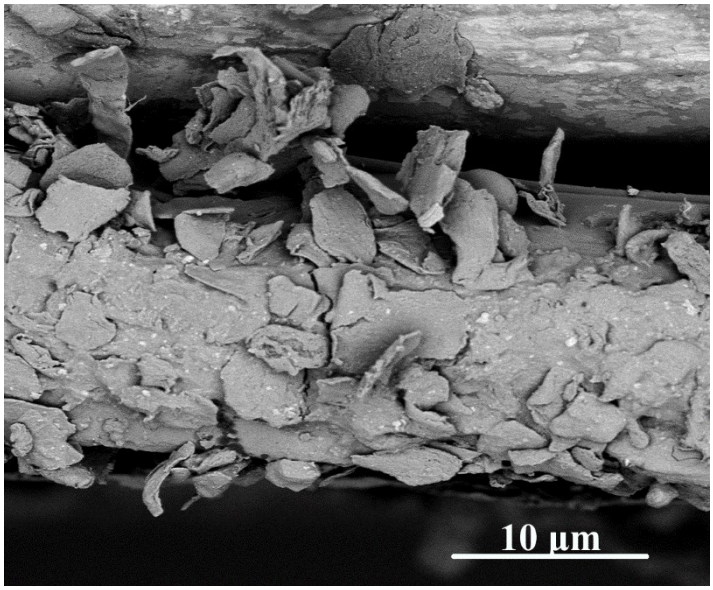

Fig. S1 The cross-sectional SEM image of GF.

4. XPS spectra of CSO@GF and Co_3O_4@GF

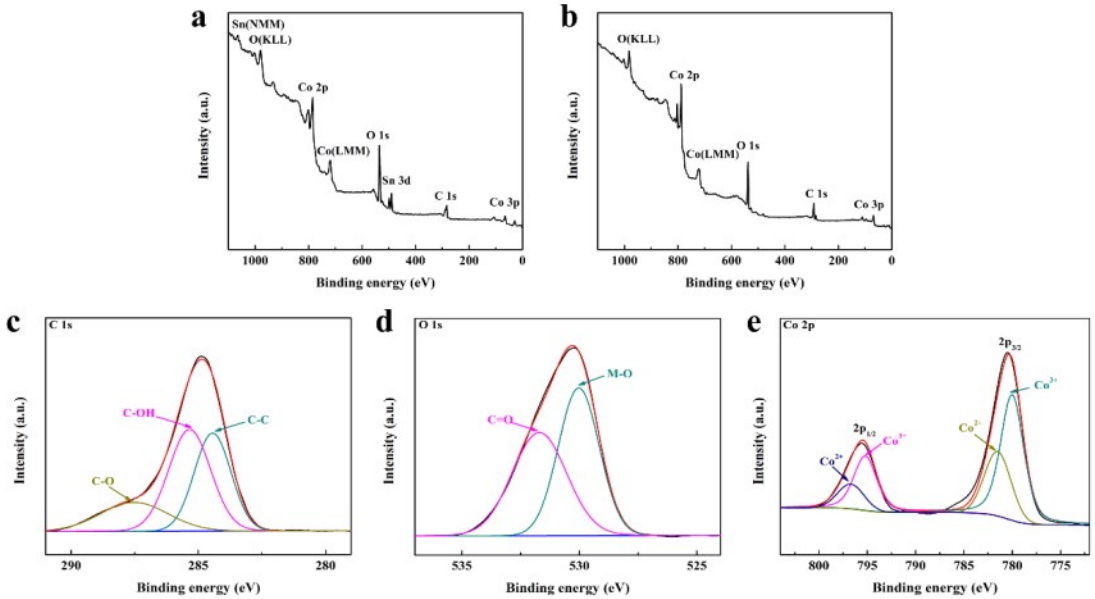

Fig. S2 The full survey XPS spectrum of (a) CSO@GF, (b) Co_3O_4@GF, XPS spectra for (c) C 1s, (d) O 1s, and (e) Co 2p.

As shown in the Co 2p spectrum of the Co_3O_4@GF sample (Fig. S2e), the atomic ratio of Co^{2+}: Co^{3+} in the sample is evaluated to be 1:2. Nevertheless, the CSO@GF sample possesses a Co^{2+}: Co^{3+} atomic ratio of 1:2.86 which is discussed in the manuscript, implying that Sn^{2+}/Sn^{4+} ions have been doped into Co_3O_4.

5. SEM images of GF and Co_3O_4@GF

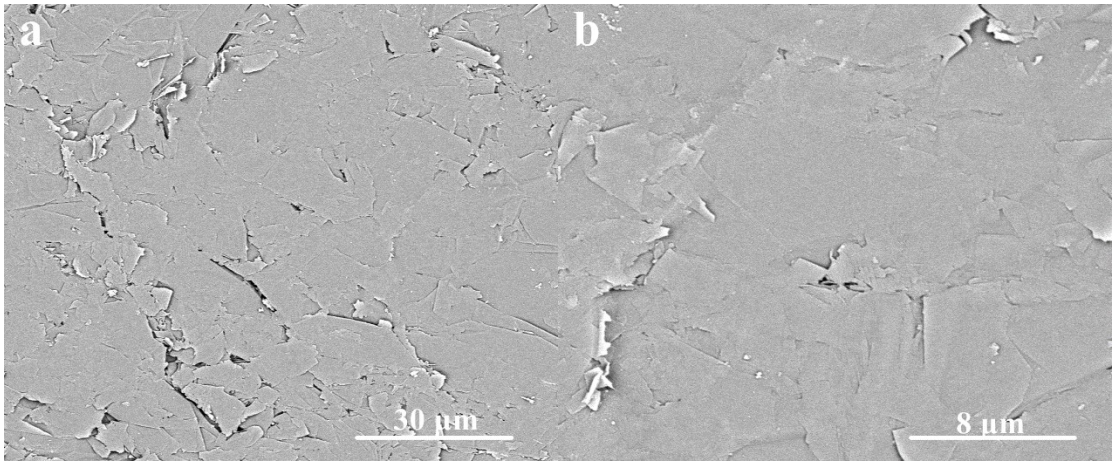

Fig. S3 SEM images of GF.

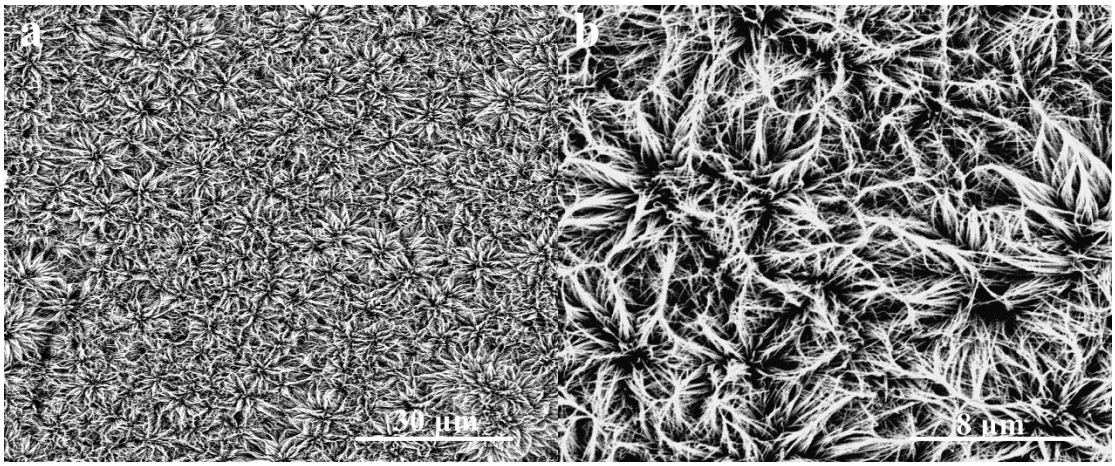

Fig. S4 SEM images of Co_3O_4@GF.

6. N_2 adsorption-desorption isotherms and pore size distribution of GF, Co_3O_4@GF, and CSO@GF

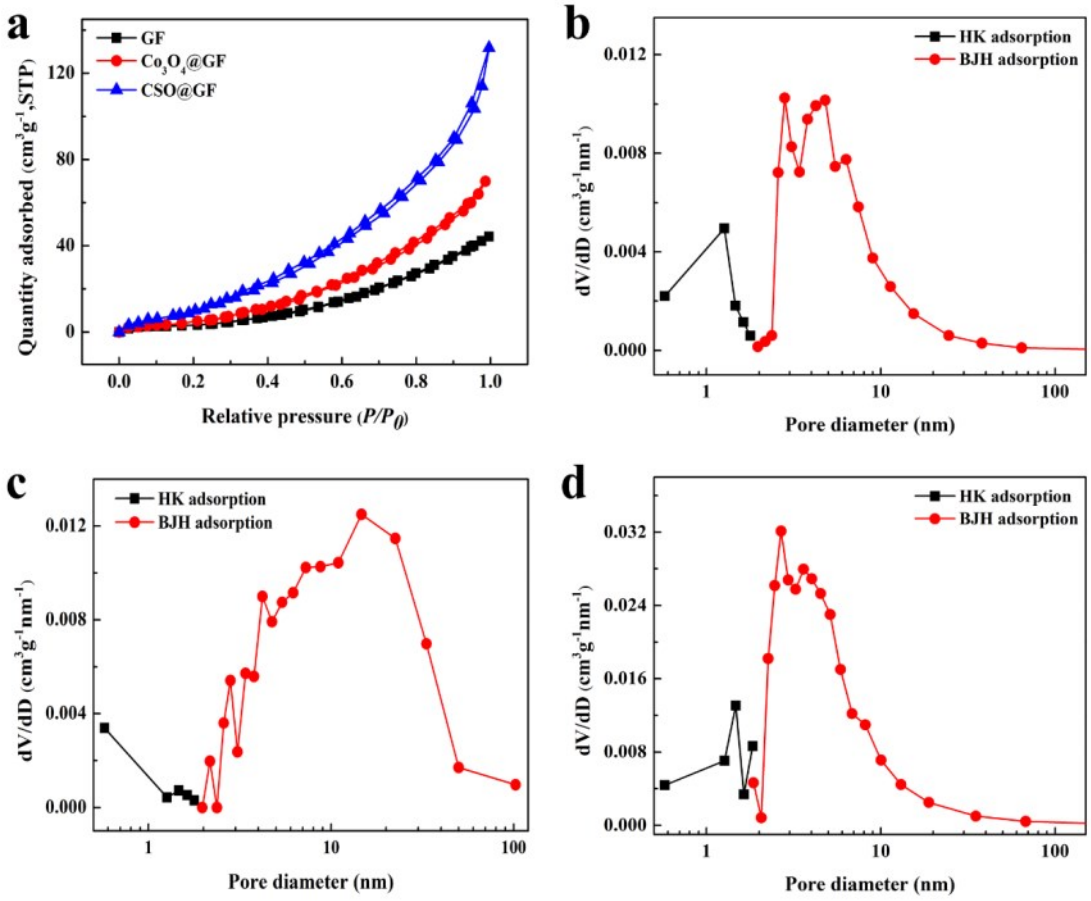

Fig. S5. (a) N_2 adsorption-desorption isotherms of GF, Co_3O_4@GF, and CSO@GF. The pore size distribution of the (b) GF, (c) Co_3O_4@GF, and (d) CSO@GF samples.

7. Characterizations of CSO@GF with different Co/Sn ratios

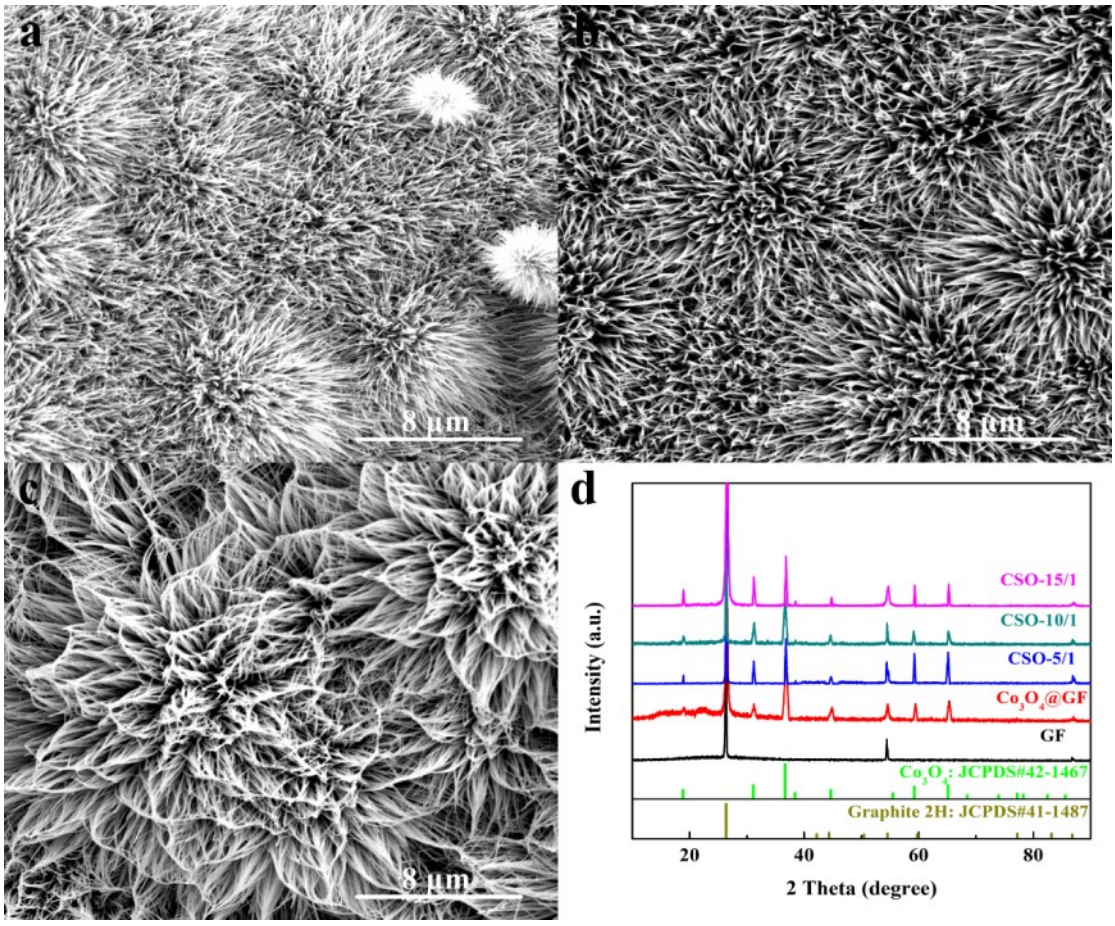

Fig. S6. SEM images of (a) CSO@GF 5-1, (b) CSO@GF 10-1, (c) CSO@GF 15-1. XRD patterns of GF, Co_3O_4@GF, CSO@GF 5-1, CSO@GF 10-1, and CSO@GF 15-1.

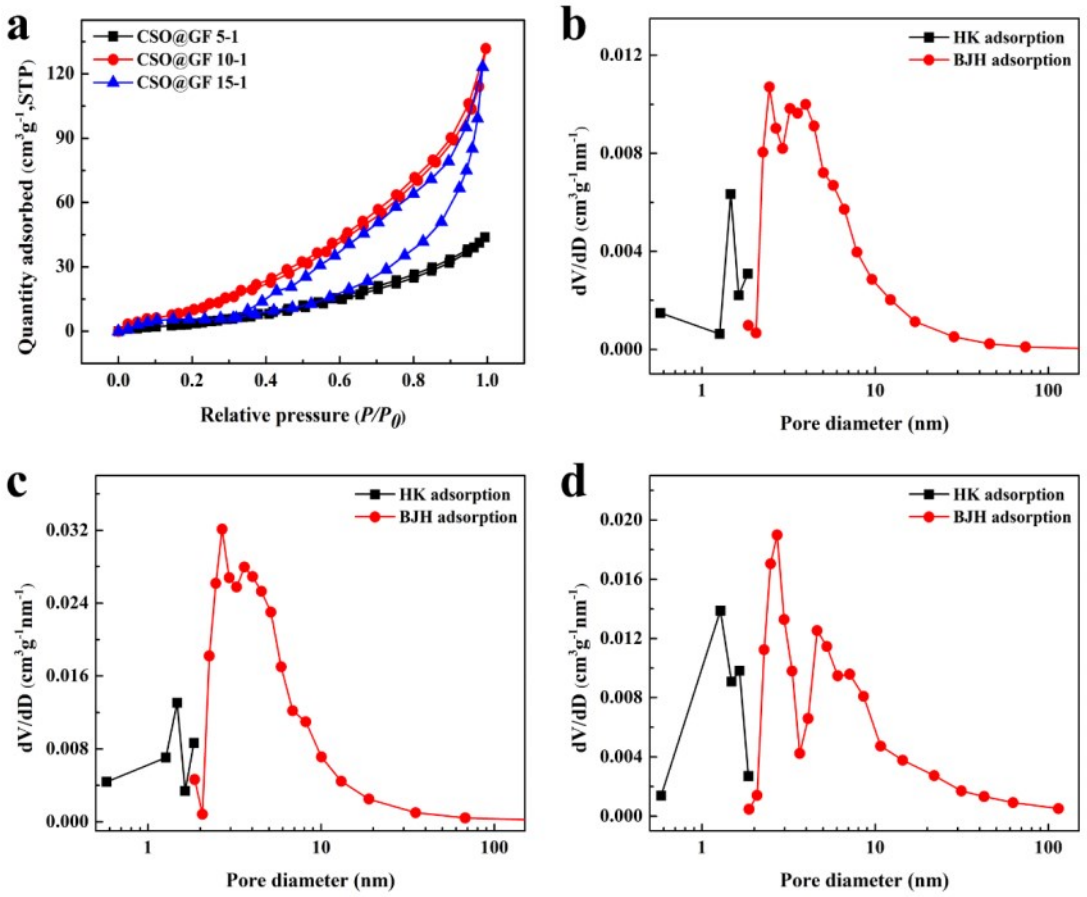

Fig. S7 (a) N_2 adsorption-desorption isotherms of CSO@GF 5-1, CSO@GF 10-1 and CSO@GF 15-1, HK adsorption and BJH pore size distribution curves of (b) CSO@GF 5-1, (c) CSO@GF 10-1 and (d) CSO@GF 15-1.

8. CV curves of CSO@GF with different Co/Sn ratios

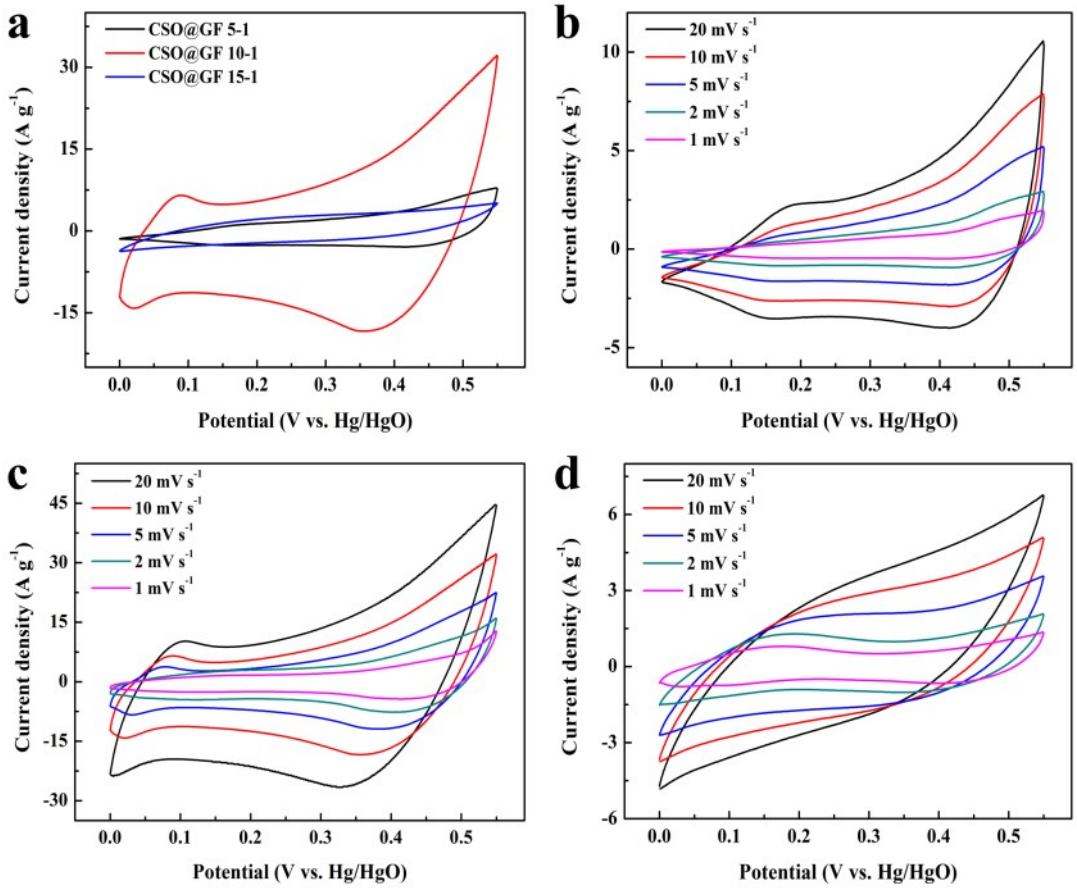

Fig. S8 (a) CV curves at scan rate of 10 mV s^{-1} for CSO@GF 5-1, CSO@GF 10-1, and CSO@GF 15-1, respectively. CV curves at different scan rates for (b) CSO@GF 5-1, (c) CSO@GF 10-1 and (d) CSO@GF 15-1, respectively.

From the CV curves of three samples (Fig. S8a), the CV curve of the CSO@GF 10-1 electrode exhibits a maximal integral area, suggesting an optimal capacitance.

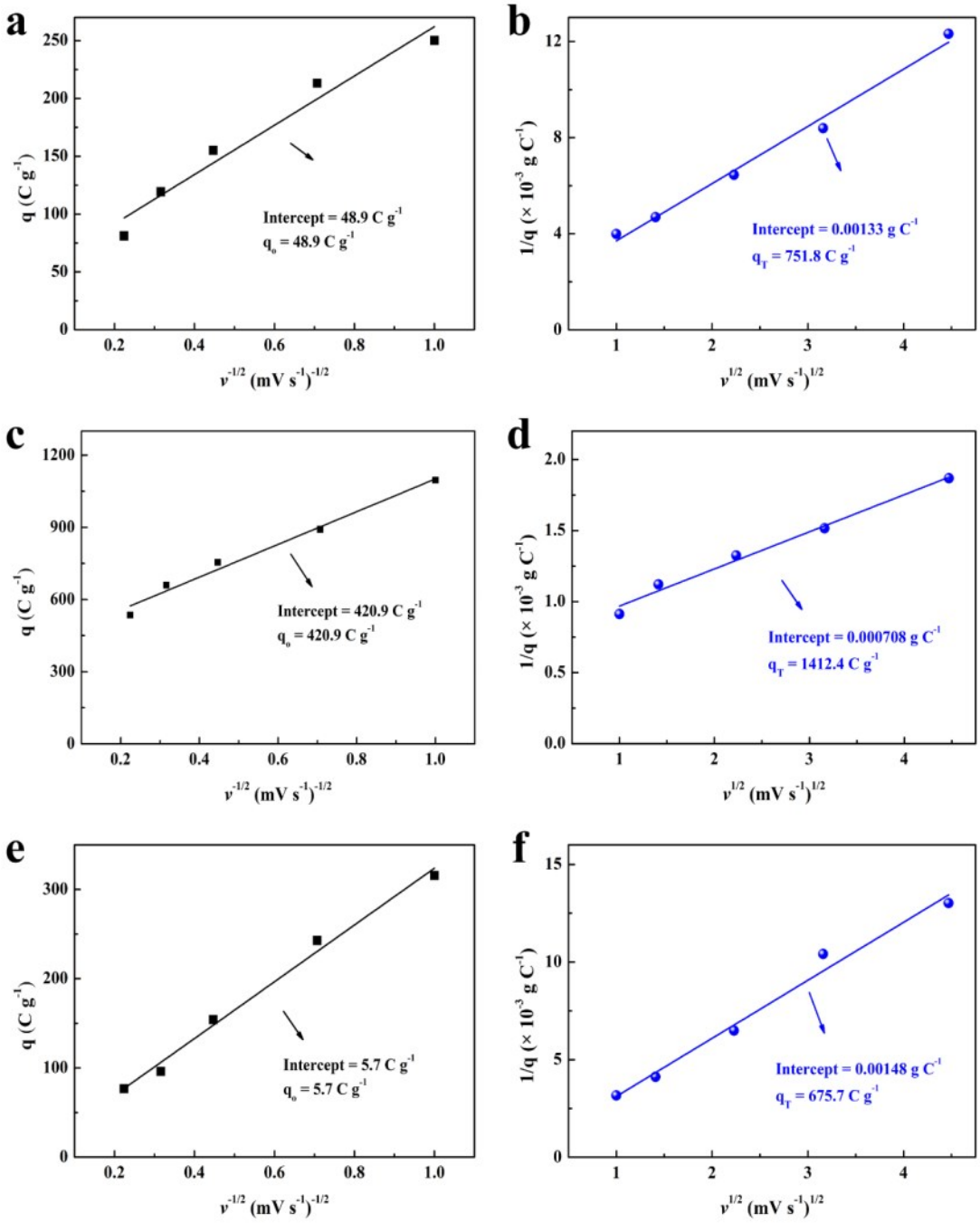

Fig. S9 Variation of the voltammetric charge (q) with respect to the potential scan rates *v*: plot of q vs $v^{-1/2}$ (extrapolation of q to $v = \infty$ gives the outer charge q_o) of (a) CSO@GF 5-1, (c) CSO@GF 10-1 and (e) CSO@GF 15-1, respectively. Plot of 1/q vs $v^{1/2}$ (extrapolation of q to $v = 0$ gives the total charge q_T) of (b) CSO@GF 5-1, (d) CSO@GF 10-1 and (f) CSO@GF 15-1, respectively.

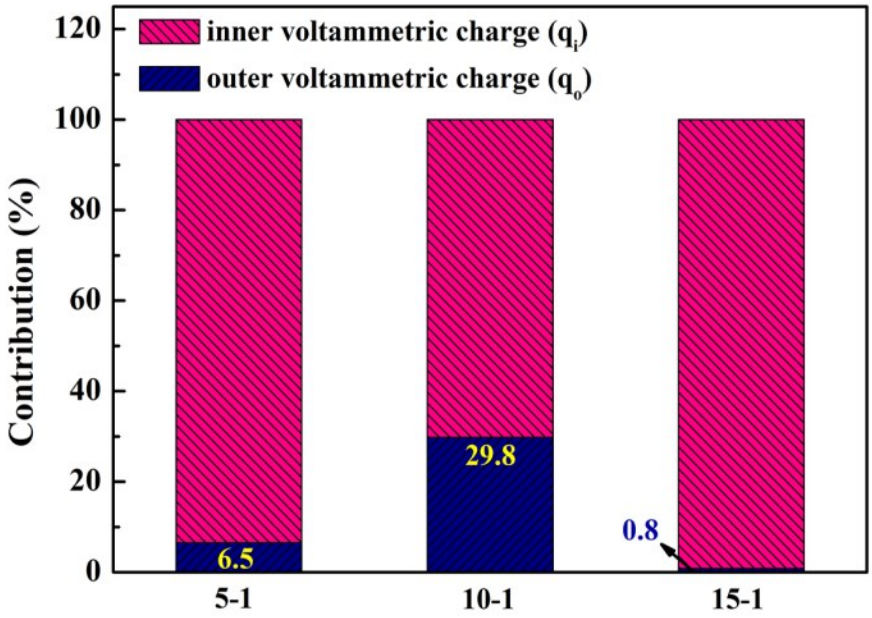

Fig. S10. Relative contributions of inner and outer voltammetric charge storage process of CSO@GF 5-1, CSO@GF 10-1, and CSO@GF 15-1.

Table S1. The q_o and q_T of the samples.

Sample (C g^{-1})	CSO@GF 5-1	CSO@GF 10-1	CSO@GF 15-1
q_o	48.9	420.9	5.7
q_T	751.8	1412.4	675.
q_o/q_T	6.5%	29.8%	0.8%

The voltammetric charge (q) was calculated by the integral area of CV curves at various scan rates. The q_o, denoting the accessible outer surface for ions at high scan rates, was determined by extrapolating the scan rate to infinity. The q_T, which corresponds to all the charge surface at slow scan rates, was calculated by the extrapolation of q to $v = 0$. Besides, the inner voltammetric charge, which indicates the inaccessible active surface, could be estimated from the difference between q_o and q_T. Thus, the ratio of q_o/q_T for CSO@GF 10-1 (29.8%) was significantly larger than those for CSO@GF 5-1 (6.5%) and CSO@GF 10-1 (0.8%), indicating CSO@GF 10-1 has more electrochemically active surface area, which is available for ion diffusion during the redox reaction.

9. GCD curves of CSO@GF with different Co/Sn ratios

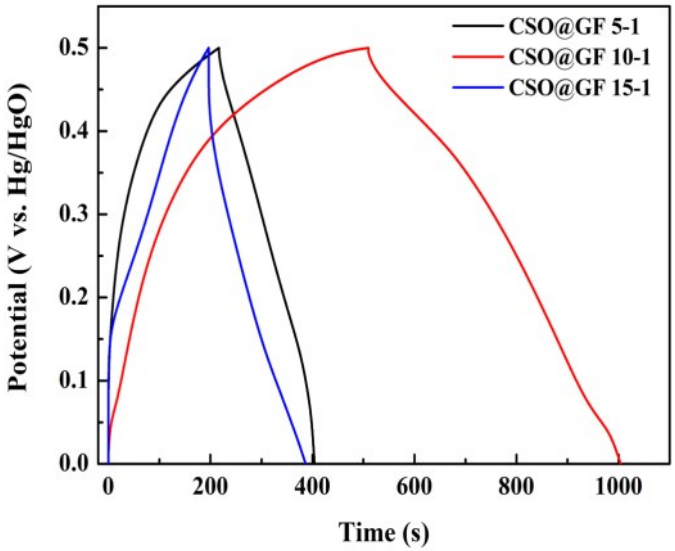

Fig. S11. GCD curves at current density of 2 A g^{-1} for CSO@GF 5-1, CSO@GF 10-1, and CSO@GF 15-1.

It can be seen that the capacitance of CSO@GF 10-1 is larger than those of other electrodes, implying that the CSO@GF electrode is more suitable than other electrodes for supercapacitors.

10. Electrochemical performance of CSO@GF with different Co/Sn ratios

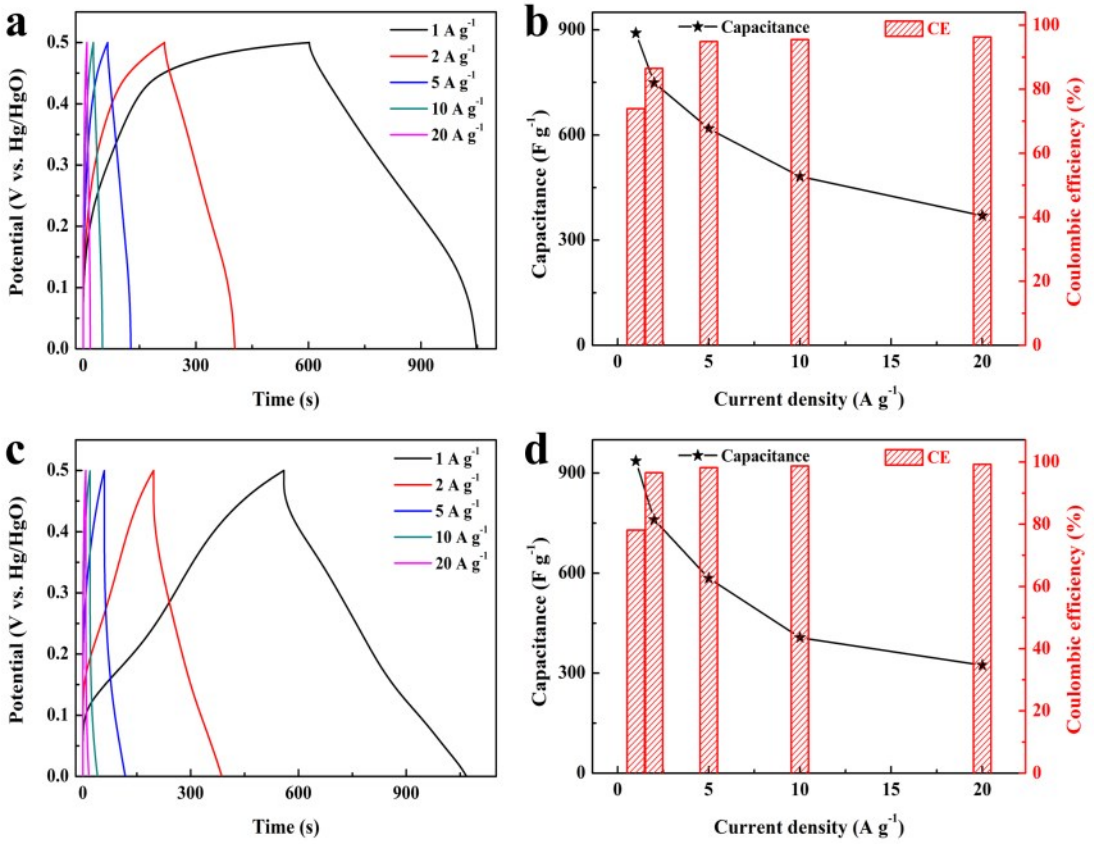

Fig. S12. GCD curves at various current densities for (a) CSO@GF 5-1 and (c) CSO@GF 15-1, respectively. (d) The specific capacitances and Coulombic efficiency of the CSO@GF 5-1 and CSO@GF 15-1 electrode at different current densities.

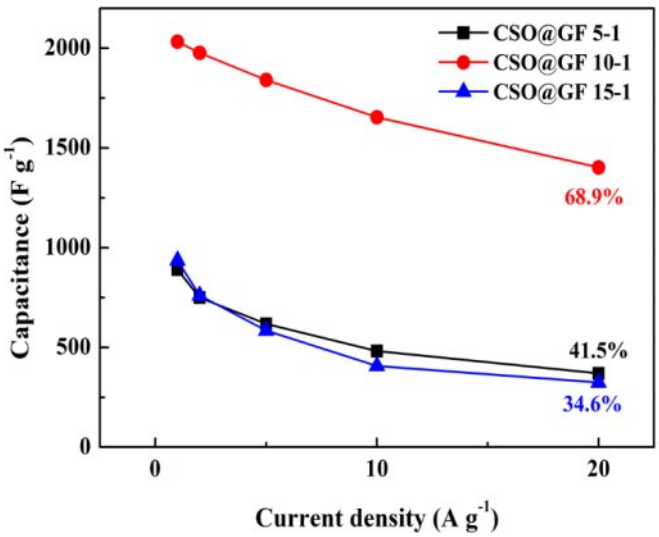

Fig. S13 The specific capacitances of CSO@GF 5-1, CSO@GF 10-1, and CSO@GF 15-1 at different current densities.

Table S2. Specific capacitance and retention of samples.

Sample	CSO@GF	CSO@GF 10-1	CSO@GF 15-1
specific capacitance	890.8 F g^{-1}	2032.6 F g^{-1}	936.4 F g^{-1}
specific capacity	445.4 C g^{-1}	1016.3 C g^{-1}	468.2 C g^{-1}
retention	41.5%	68.9%	34.6%

As concluded from Fig. S11-S13 and Tab. S2, 10:1 (Co: Sn) is the optimal ratio to prepare CSO@GF.

11. Nyquist plots of CSO@GF with different Co/Sn ratios

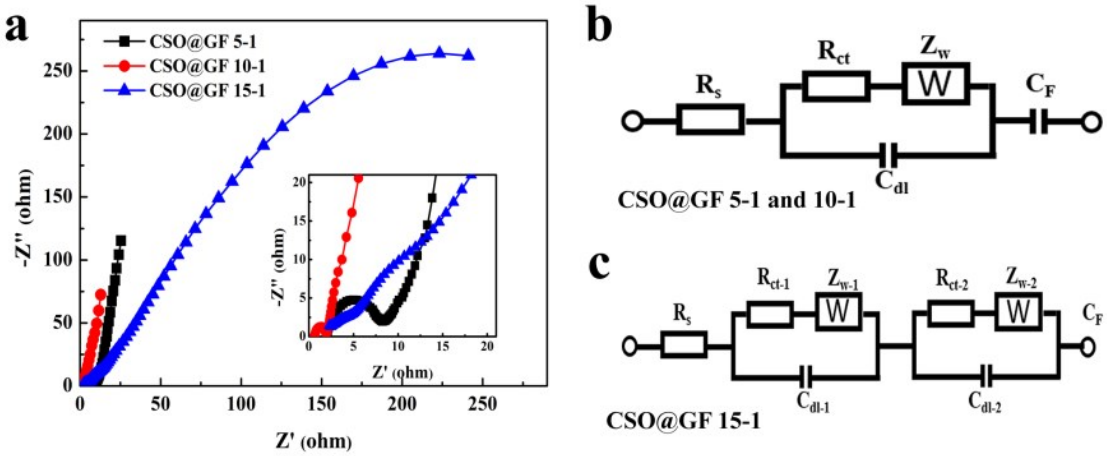

Fig. S14. (a) Nyquist plots of CSO@GF 5-1 CSO@GF 10-1 and CSO@GF 15-1 electrodes, and the equivalent circuit model of (b) CSO@GF 5-1 and 10-1 and (c) CSO@GF 15-1.

12. Electrochemical performance comparison of hydrothermal samples before and after heat treatment

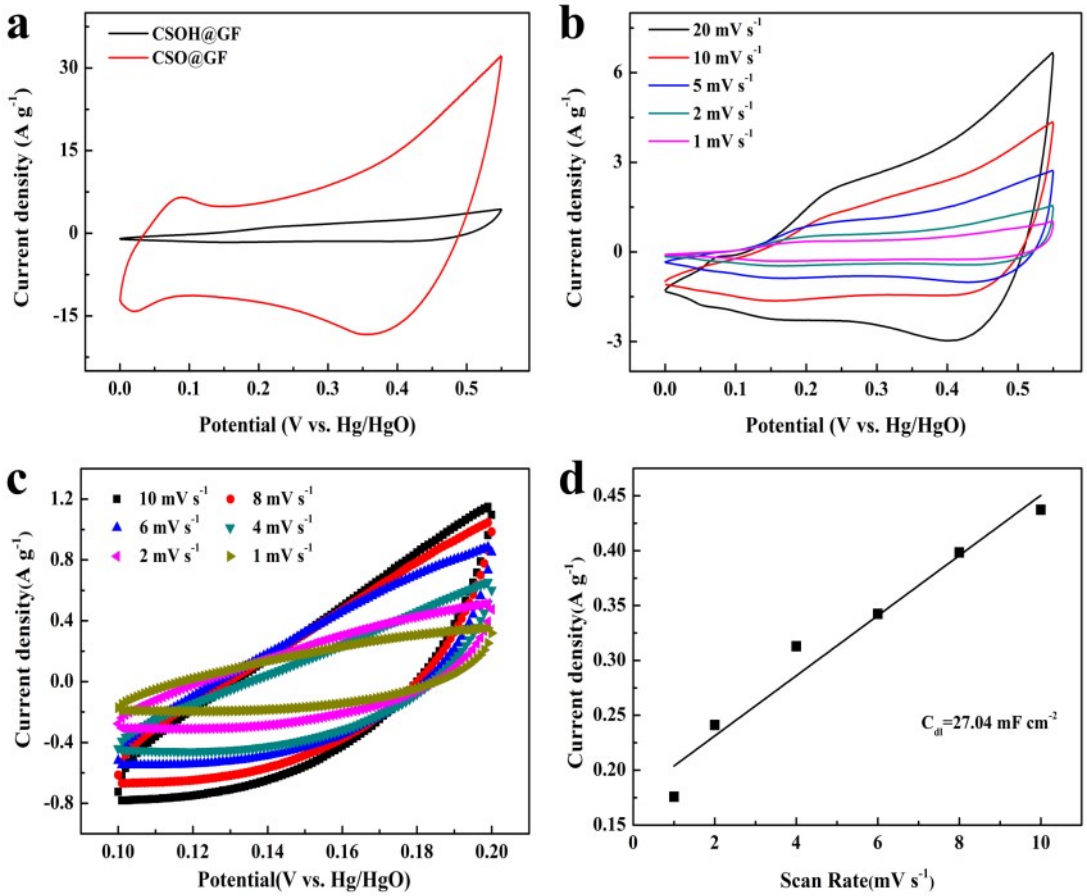

Fig. S15. (a) CV curves at 10 mV s^{-1} for Co/Sn hydroxide coated on graphane film (CSOH@GF) and CSO@GF, respectively, (b) CV curves at different scan rates of CSOH@GF, (c) CV curves of CSOH@GF from 0.1 to 0.2 V at different scan rates and (d) C_{dl} of CSOH@GF.

The linear plots were calculated by subtracting current density at 0.15 V (upper) from current density at 0.15 V (below), then divided by 2. The double layer capacitance (C_{dl}) value was determined from the slope of linear plots.[S1] The electrochemical active surface area (EASA, cm^2) was estimated from dividing the Cdl (μF) by 60μF cm^{-2}.[S2]

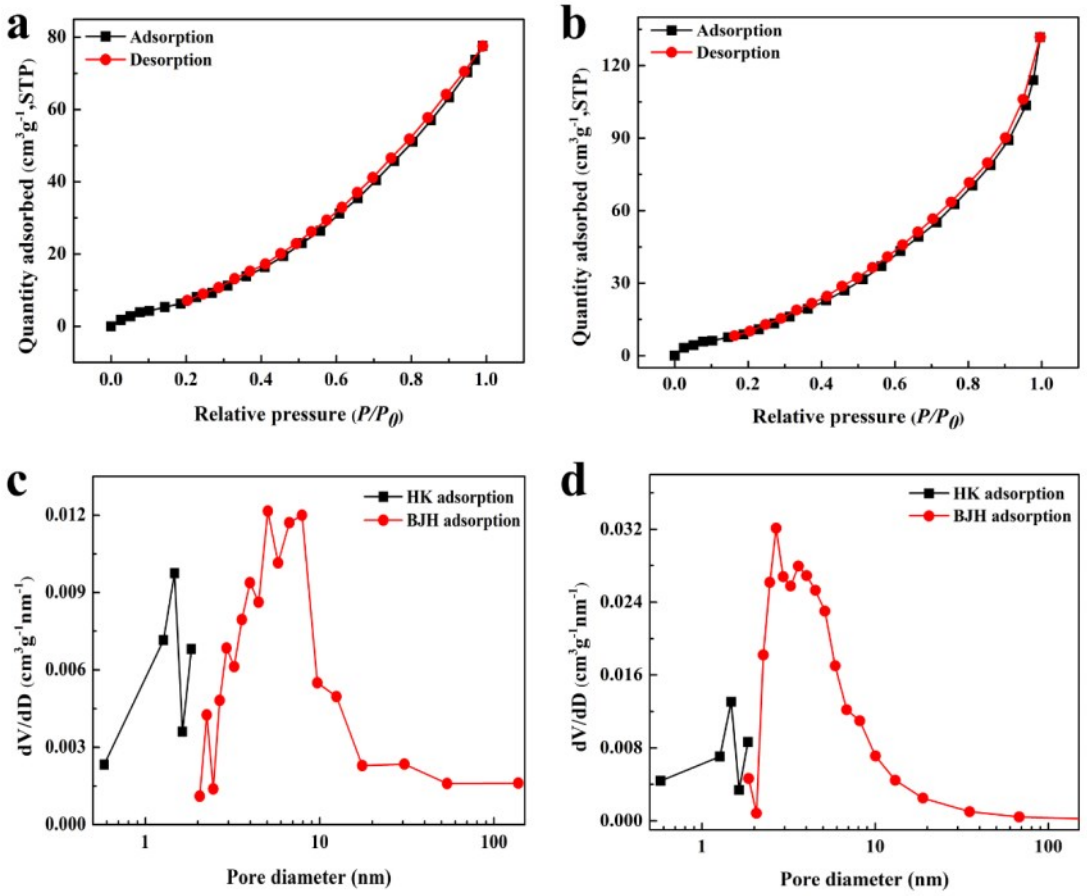

Fig. S16 N_2 adsorption-desorption isotherms of (a) CSOH@GF and (b) CSO@GF. HK adsorption and BJH pore size distribution curves of (c) CSOH@GF and (d) CSO@GF.

Table S3. EASA and SSA of samples.

sample	CSOH@GF	CSO@GF
EASA	450.67 cm^2	684.67 cm^2
SSA	39.46 m^2 g^{-1}	51.68 m^2 g^{-1}

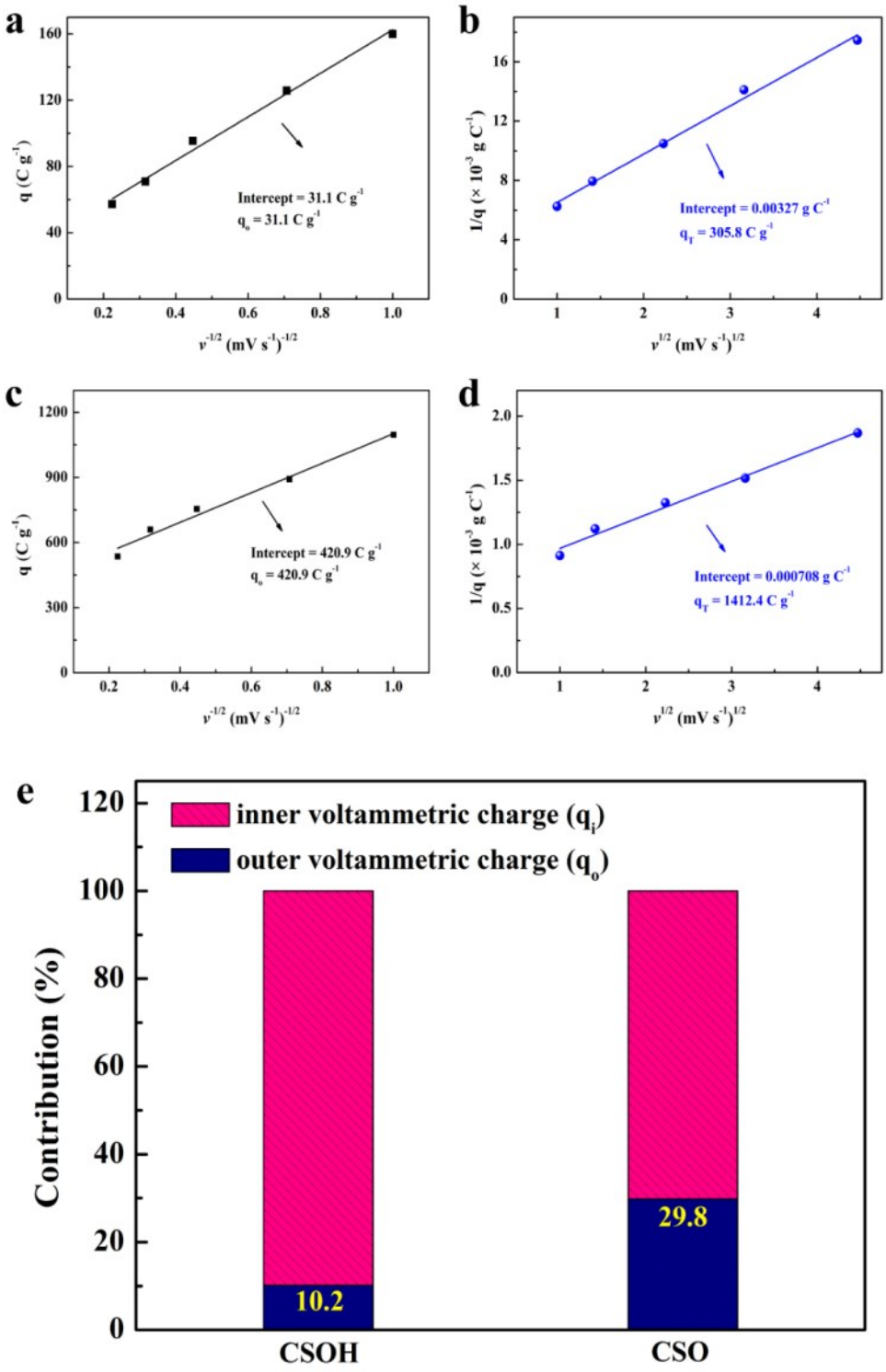

Fig. S17 Variation of the voltammetric charge (q) with respect to the potential scan rates *v*: plot of q vs $v^{-1/2}$ of (a) CSOH@GF, (c) CSO@GF, respectively. Plots of 1/q vs $v^{1/2}$ of (b) CSOH@GF and (d) CSO@GF, respectively. (e) Relative contributions of inner and outer voltammetric charge storage process of CSOH@GF and CSO@GF.

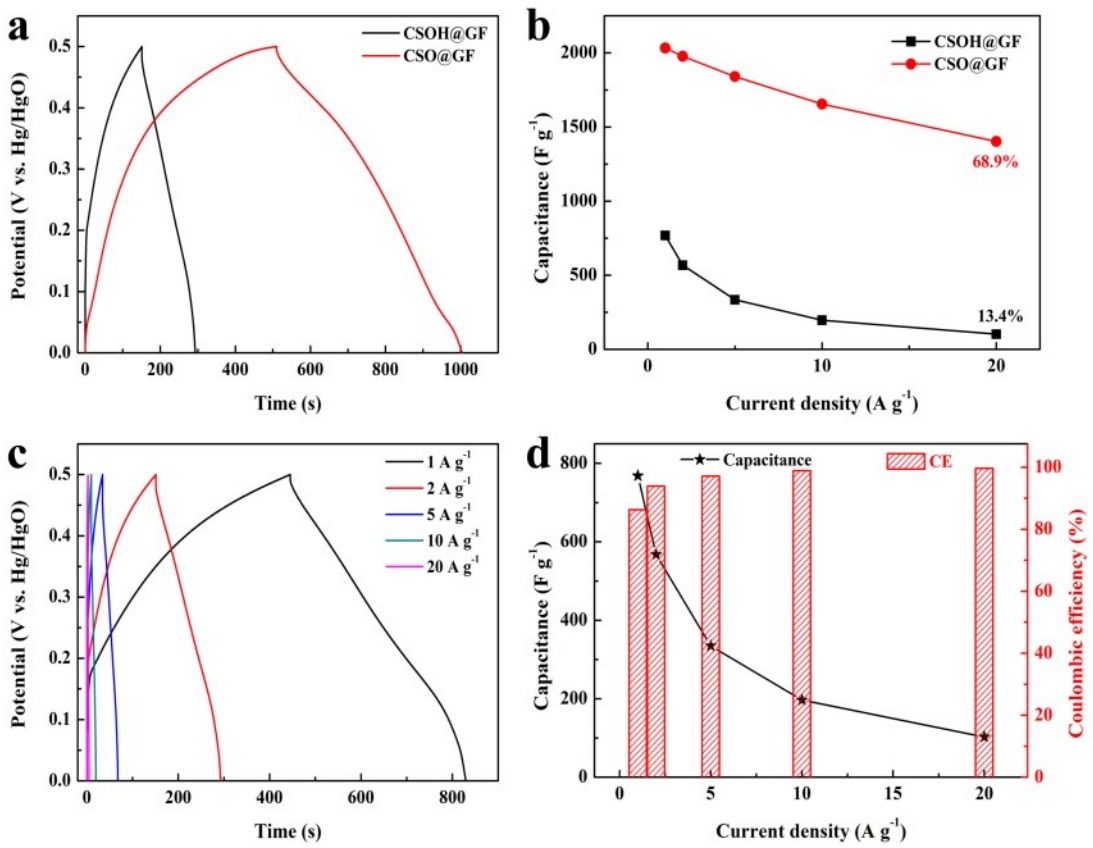

Fig. S18 (a) GCD curves at a current density of 2 A g^{-1} for CSOH@GF and CSO@GF electrodes, respectively. (b) The specific capacitance of CSOH@GF and CSO@GF at different current densities. (c) GCD curves at a series of current densities of CSOH@GF and (d) Corresponding capacitance and Coulombic efficiency of CSOH@GF.

Table S4. Specific capacitance and retention of samples.

sample	CSOH@GF	CSO@GF
q_o/q_T	10.2%	29.8%
specific capacitance	768.2 F g^{-1}	2032.6 F g^{-1}
specific capacity	384.1 C g^{-1}	1016.3 C g^{-1}
retention	13.4%	68.9%

As concluded from Fig. S15-S18 and Tables S3-S4, the CSO@GF possesses better electrochemical performance than the CSOH@GF sample.

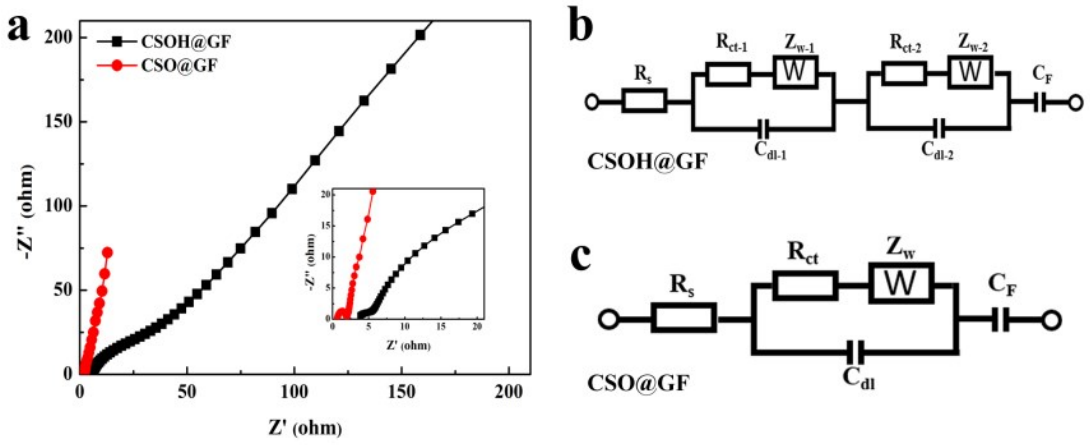

Fig. S19 (a) Nyquist plots of CSOH@GF and CSO@GF electrodes, and the equivalent circuit model of (b) CSOH@GF and (c) CSO@GF.

The R_{ct} of the CSO@GF electrode (1.31 Ω) is slower than that of CSOH@GF (2.16 Ω), indicating the CSO@GF electrode delivers better electrical conduction.

It is concluded from the results of Figs. S6-S19 and Tables S1-S4 that the CSO@GF 10-1 electrode is superior to the CSO@GF 5-1 and CSO@GF 15-1 electrode in electrochemical property, which means 10:1 is the best ratio of cobalt to the tin. In addition, the annealing procedure leads the CSOH@GF change to CSO@GF, which further improves the electrochemical performance.

13. Electrochemical performance comparison of GF, Co_3O_4@GF, and CSO@GF samples

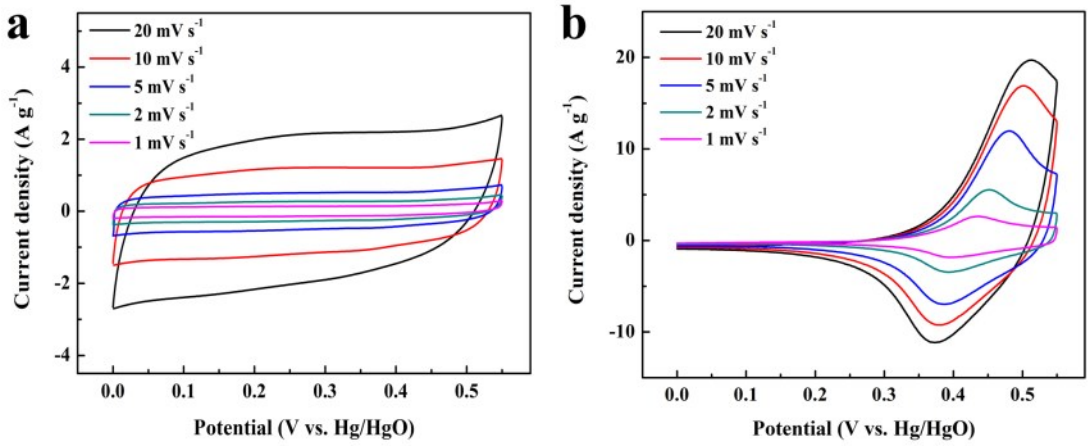

Fig. S20 CV curves of (a) GF and (b) Co_3O_4@GF at different scan rates.

The typical CV curves of Co_3O_4@GF electrode exhibit a pair of oxidation-reduction peaks around 0.45V/0.35V, which are attributed to the conversion of cobalt oxidation states (Co_3O_4/CoOOH, CoOOH/$Co(OH)_2$) and it can be expressed [S3] as follows:

$$Co_3O_4 + OH^- + H_2O \leftrightarrow 3CoOOH + e^- \quad \text{(S1)}$$

$$Co(OH)_2 + OH^- \leftrightarrow CoOOH + H_2O + e^- \quad \text{(S2)}$$

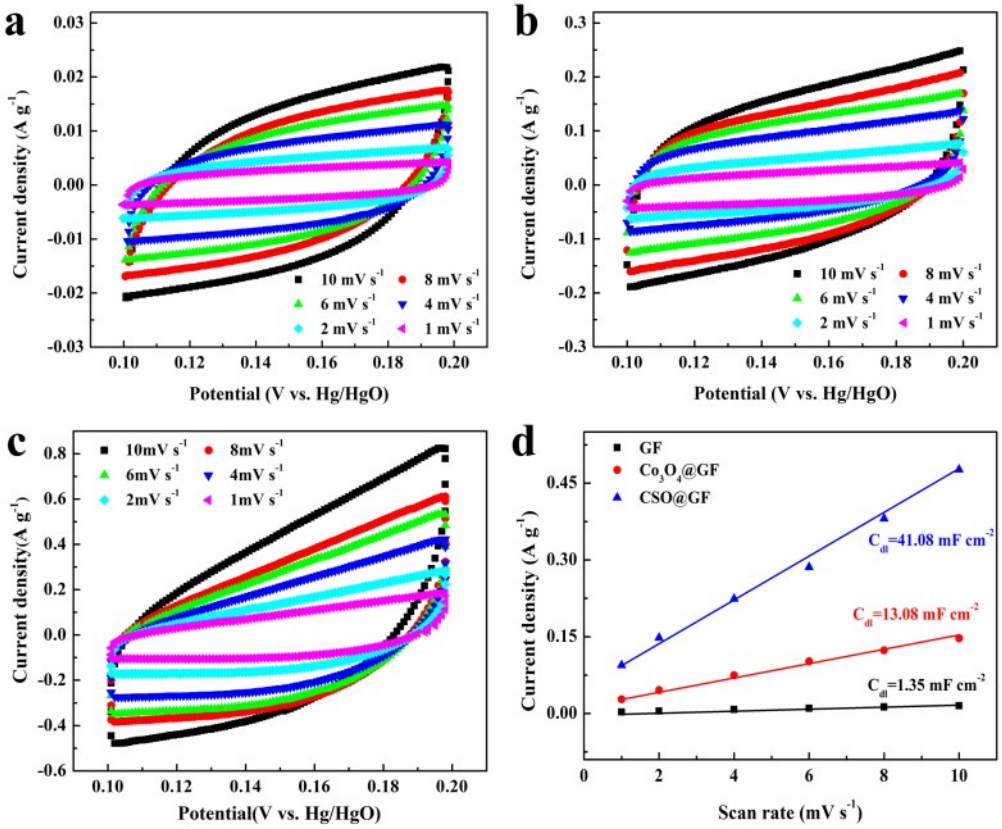

Fig. S21 CV curves from 0.1 to 0.2 V at different scan rates of (a) GF, (b) Co_3O_4@GF (c)

CSO@GF, and (d) C_{dl} values of GF, Co_3O_4@GF and CSO@GF.

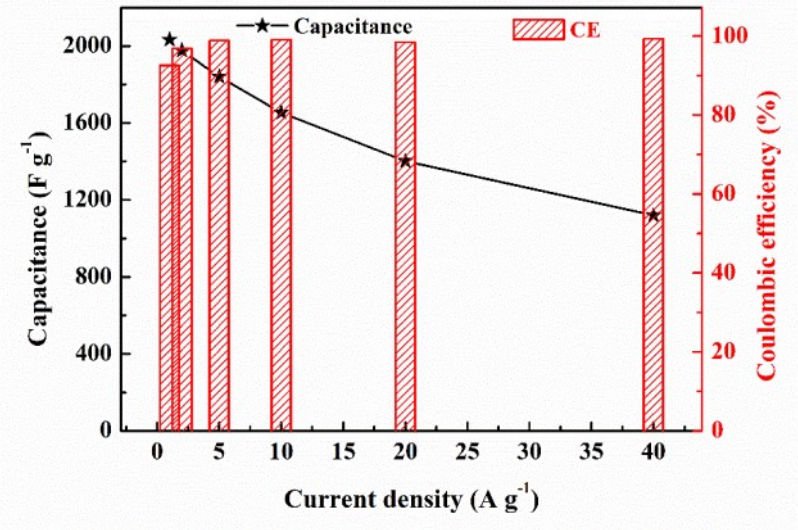

Fig. S22 The specific capacitance and Coulombic efficiency of the CSO@GF electrode at various current densities.

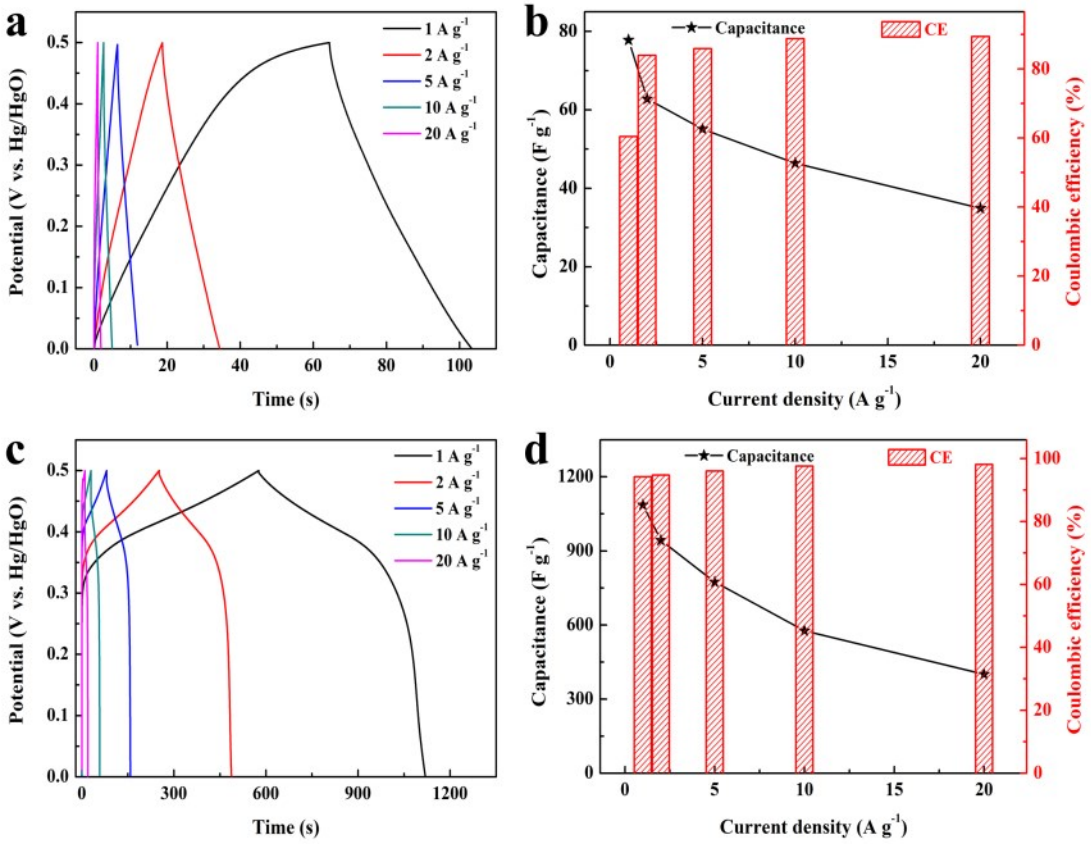

Fig. S23 GCD curves of (a) GF and (c) Co_3O_4@GF at various current densities. Corresponding specific capacitance and Coulombic efficiency of (b) GF and (d) Co_3O_4@GF.

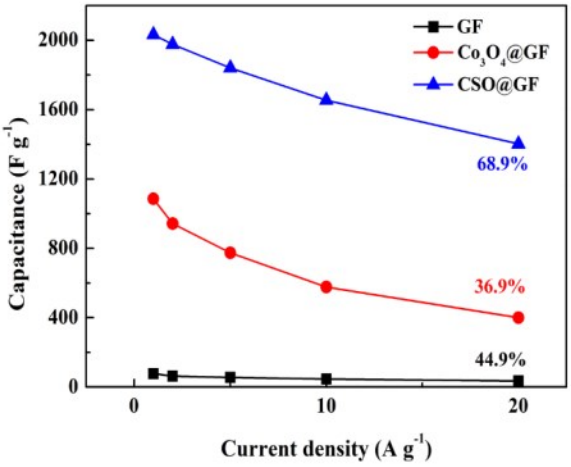

Fig. S24 Specific capacitances of GF, Co_3O_4@GF, and CSO@GF electrodes at different current densities.

14. Contributions from the capacitive and diffusion charge storage process for Co_3O_4@GF and CSO@GF samples

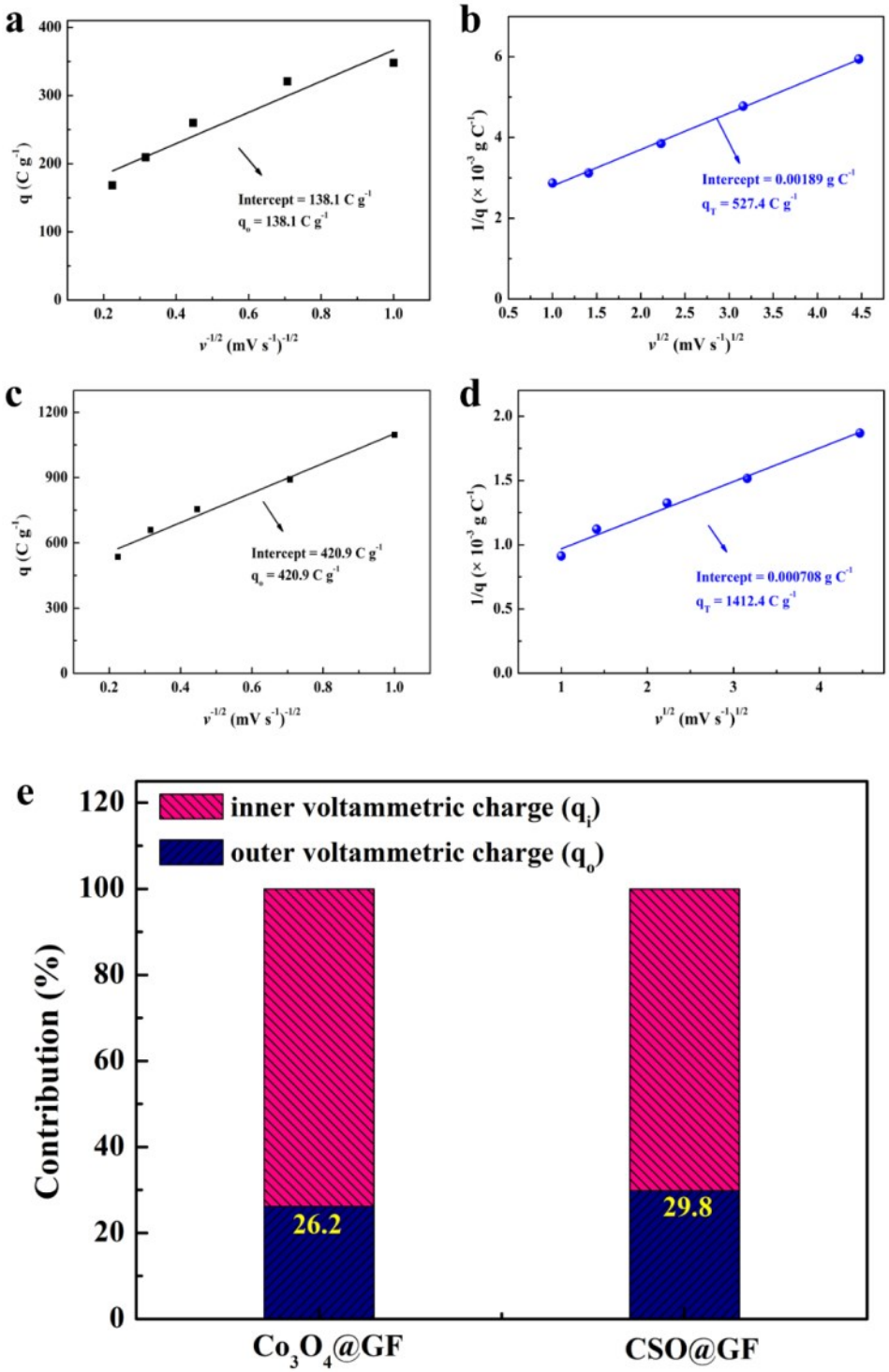

Fig. S25 Linear extrapolation of outer (a) charge q_o to $v = \infty$ and (b) total charge q_T to $v = 0$ for Co_3O_4@GF, (c) charge q_o to $v = \infty$ and (d) total charge q_T to $v = 0$ for CSO@GF, and (e) relative contributions of inner and outer voltammetric charge storage process of Co_3O_4@GF and CSO@GF.

Table S5. Contributions from the capacitive and diffusion charge storage process for samples.

sample (C g^{-1})	Co_3O_4@GF	CSO@GF
q_o	138.1	420.9
q_T	527.4	1412.4
q_o/q_T	26.2%	29.8%

As shown in Fig. S25 and Table S5, the ratio of q_o/q_T for CSO@GF was larger than that for Co_3O_4@GF, suggesting that CSO facilitated the ion migration to the electroactive surface and then promote the charge transfer reactions. It was observed that the contributions of the diffusion-controlled process gradually decreased with the increase of the scan rate (Fig. 5f), which is caused by the entry of electrolyte ions into the lattice.

15. Characterizations of Co_3O_4@GF and CSO@GF after the long-term GCD cycles

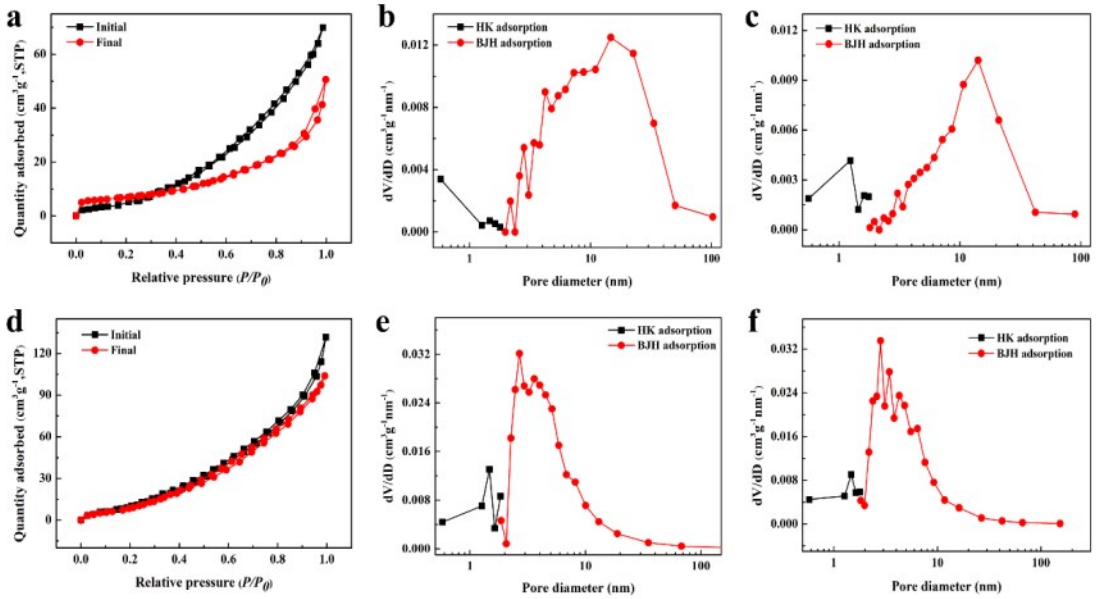

Fig. S26 N_2 adsorption-desorption isotherms of (a) Co_3O_4@GF (d) CSO@GF, HK adsorption and BJH pore size distribution curves of Co_3O_4@GF (b) initial and (c) final, CSO@GF (e) initial and (f) final.

16. Characterizations of Fe_2O_3@GF sample

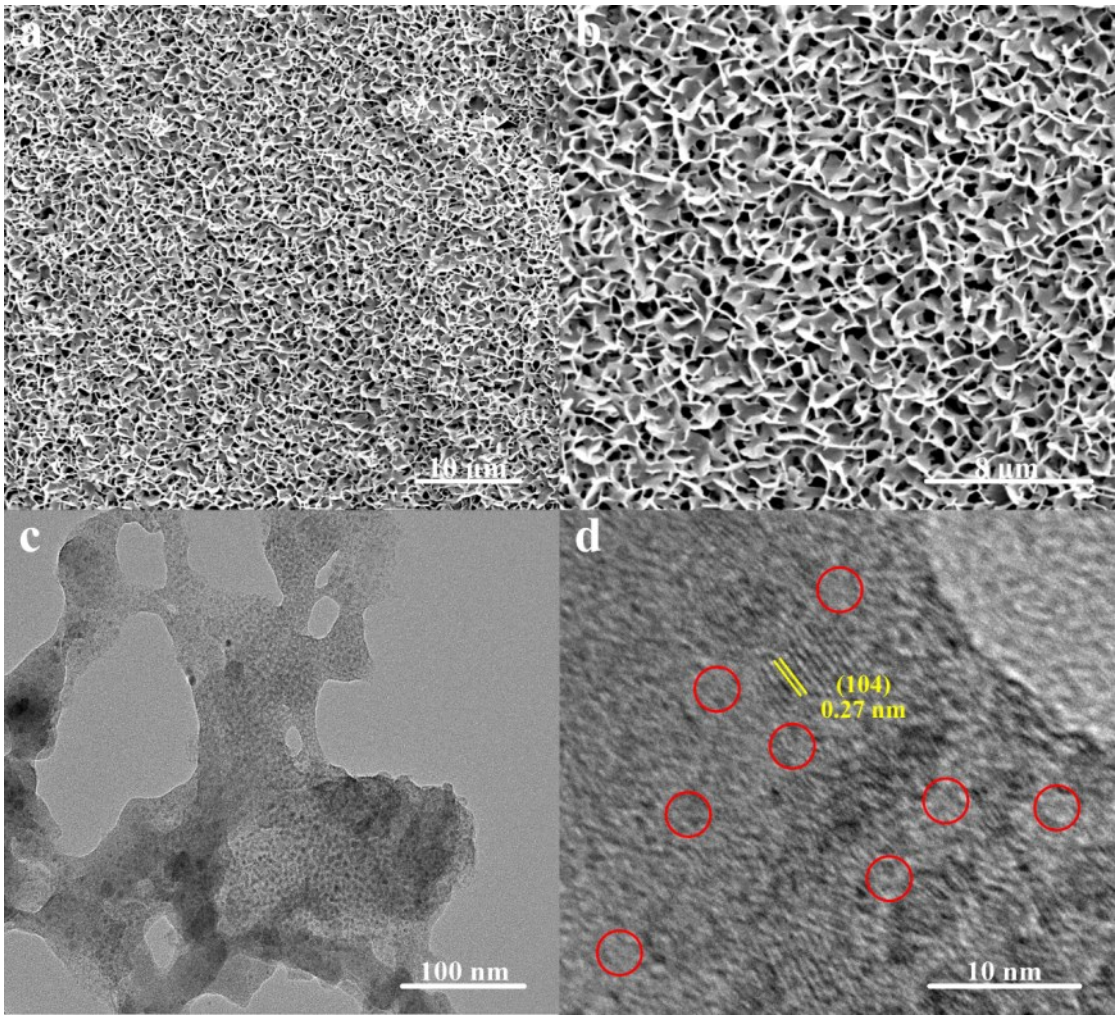

Fig. S27 (a) and (b) SEM images of Fe_2O_3@GF, (c), and (d) TEM images of Fe_2O_3@GF.

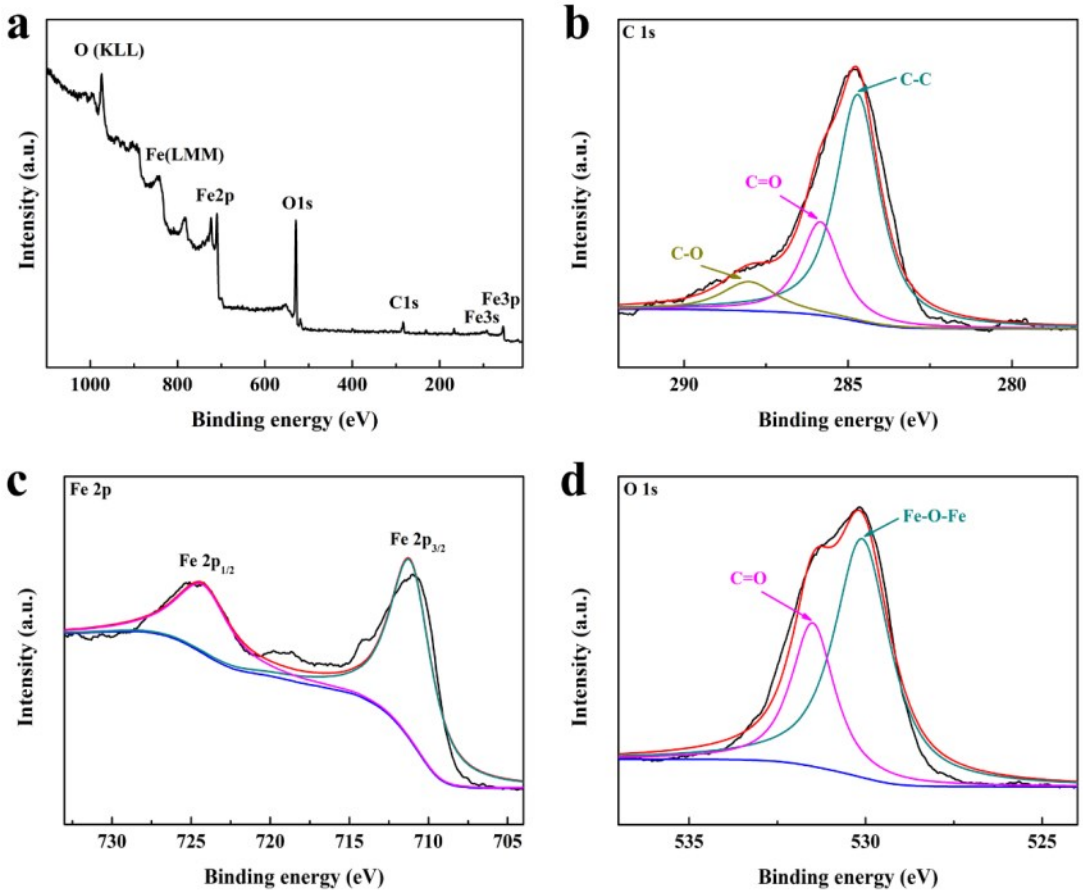

Fig. S28 (a) The full survey XPS spectrum of Fe_2O_3@GF and XPS spectra for (b) C 1s, (c) Fe 2p, and (d) O 1s, respectively.

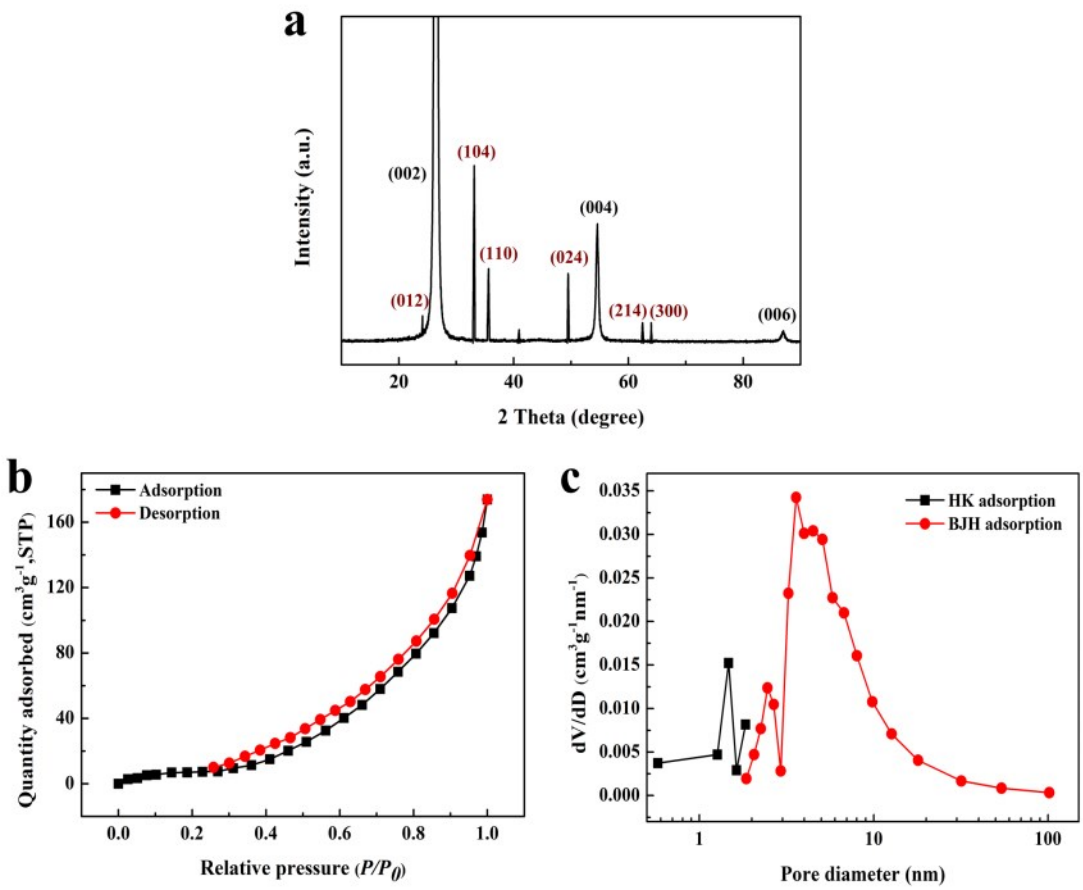

Fig. S29 (a) XRD patterns of Fe_2O_3@GF, (b) N_2 adsorption/desorption isotherms, and (c) pore size distributions of Fe_2O_3@GF.

17. Electrochemical performance of Fe_2O_3@GF sample

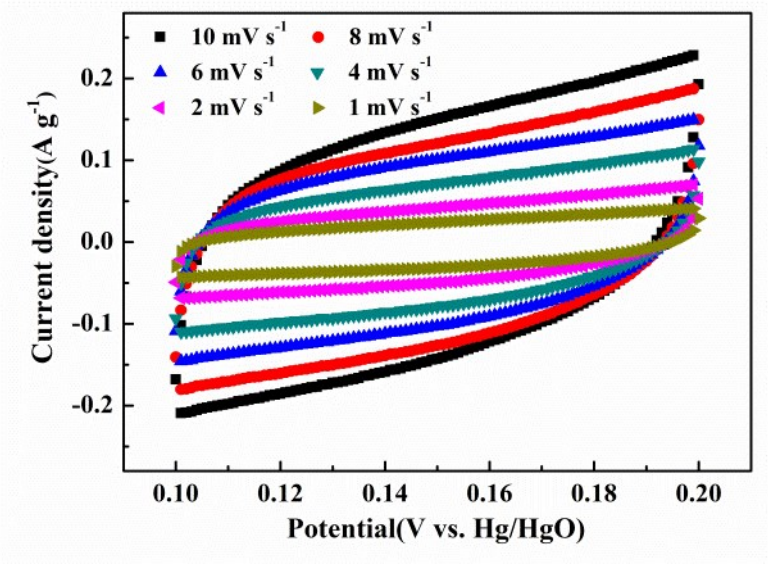

Fig. S30 CV curves from 0.1 to 0.2 V at a different scan rates of Fe_2O_3@GF.

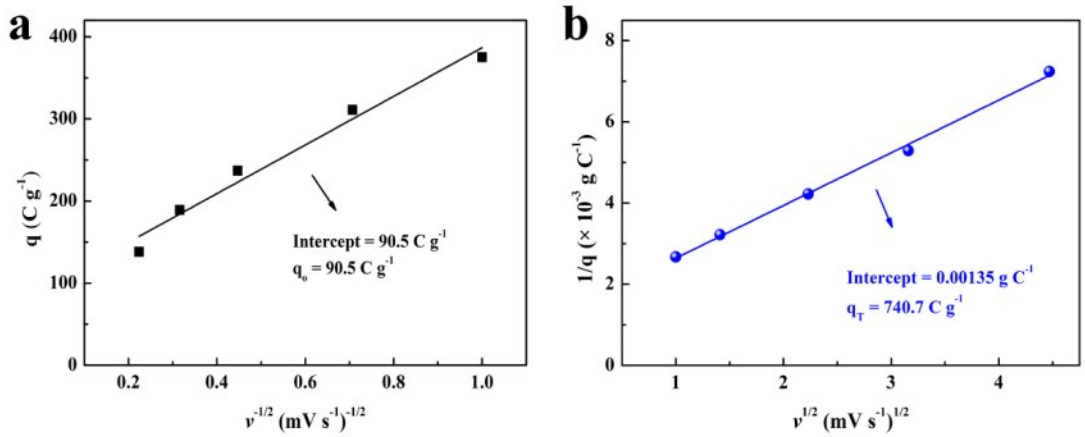

Fig. S31 Linear extrapolation of (a) outer charge q_o to $v = \infty$ and (b) total charge q_T to $v = 0$ for Fe_2O_3@GF sample.

18. Characterization of Fe_2O_3@GF sample after the long-term GCD cycles

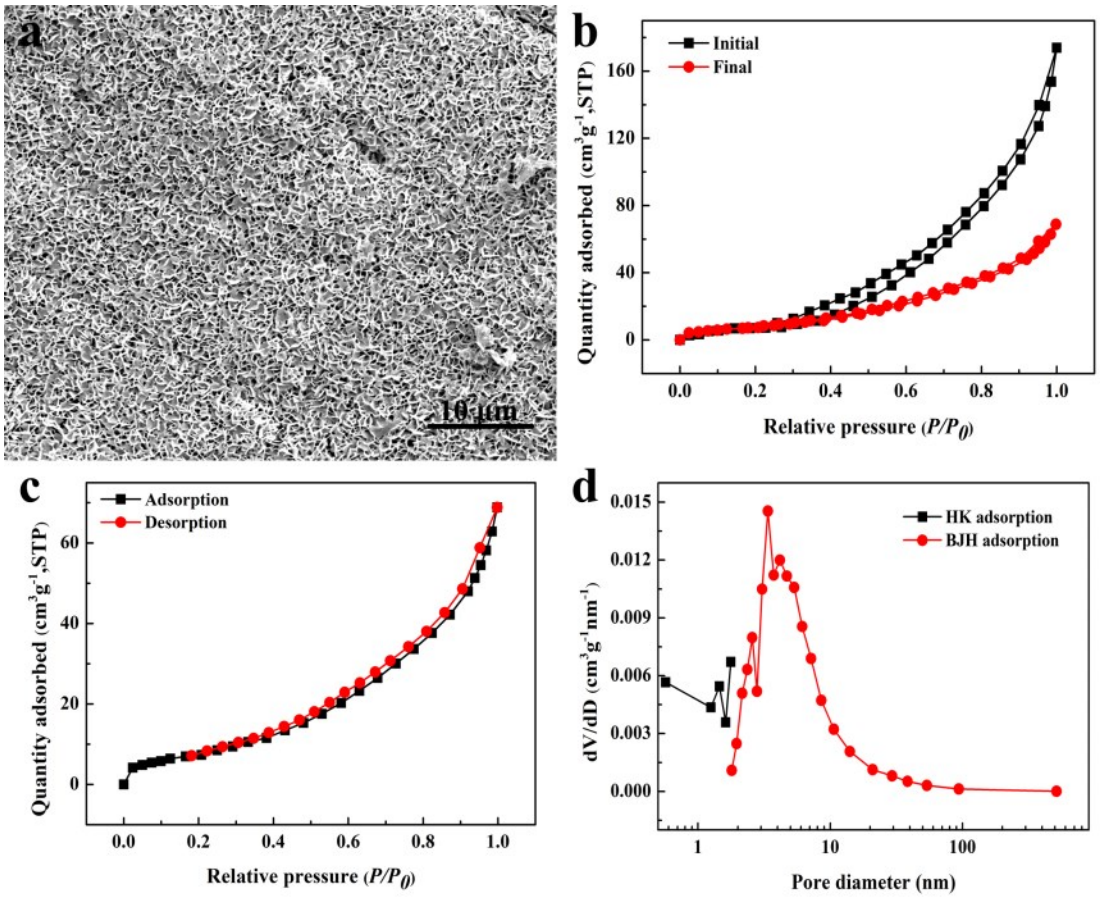

Fig. S32 (a) SEM image of Fe_2O_3@GF after cyclic test, (b) and (c) N_2 adsorption/desorption isotherms of Fe_2O_3@GF before and after the cyclic test (d) HK adsorption and BJH pore size distributions of Fe_2O_3@GF after the cyclic test.

19. Electrochemical performance characteristics of ASC device before and after cycling test

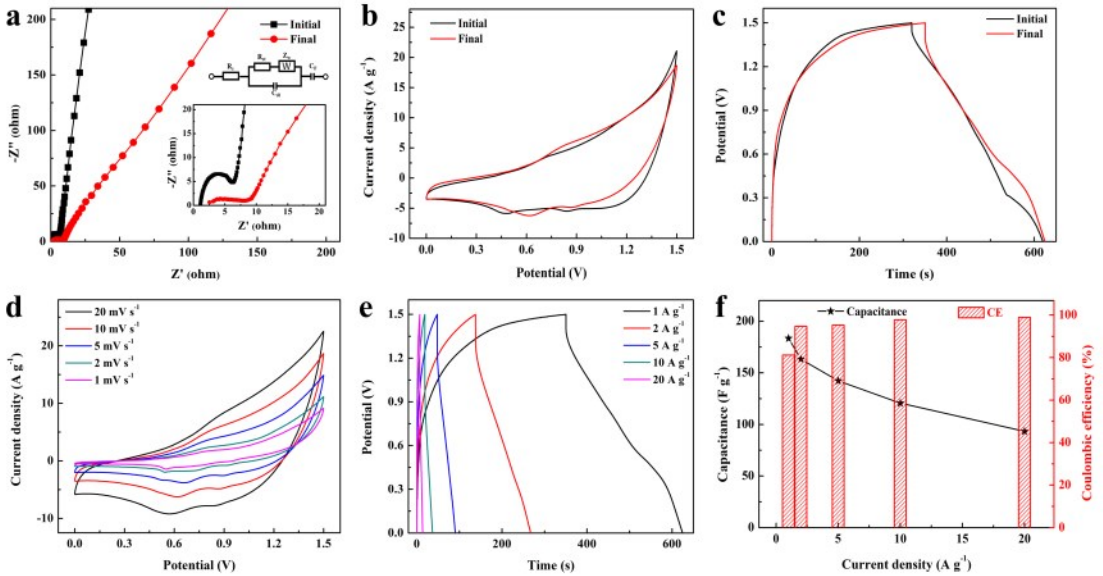

Fig. S33 Electrochemical performance characteristics of ASC device before and after cycling test (a) The Nyquist plots, inset figure of equivalent circuit, (b) CV curves at 10 mV s^{-1}, (c) GCD curves at 1 A g^{-1}. Electrochemical performance characteristics of ASC device after cycling test (d) CV curves at different scan rates, (e) GCD curves from 1 to 20 A g^{-1} and (f) The corresponding calculated capacitance and CE at different current densities.

Fig. S33a reveals the Nyquist plots of the device before and after the repeated GCD test. After 20000 cycles, the R_{ct} (17.4 Ω) became larger than that of initial (6.6 Ω) and the declined slope of the line is confirmed but still greater than 45°, which refers to the decresed capacitance. As shown in Fig. S33b, the integral area of the final CV curve at 10 mV s^{-1} has slightly decreased due to the increased impedance. From the GCD curves at 1 A g^{-1} of the device before and after the cyclic test (Fig. S33c), the specific capacitance is calculated to be 183.4 F g^{-1}, which is slightly less than the initial capacitance (200.2 F g^{-1}). The inflection points still match the CV results well. Fig. 9d-9f shows the electrochemical performance of the device after the long-term cyclic testing. The CV curves at different scan rates (Fig. S33d) are consistent with previous results (Fig. 8d), indicating the device holds the same redox reaction process. From the GCD curves (Fig. S33e) at various current densities, it can be further confirmed that the process is a redox reaction process through non-linear discharge lines, which is in accordance with the CV results. The corresponding calculated specific

capacitances are 183.4, 163.2, 142.3, 120.7, and 93.3 F g^{-1} at current densities of 1, 2, 5, 10, and 20 A g^{-1}, respectively (Fig. S33f). The capacitance retention decreased to 50.9% as the current density increased from 1 to 20 A g^{-1}, which is slightly smaller than that of the initial device (59.3%) due to the enlarged internal resistance and reduced SSA. Meanwhile, the Coulombic efficiency increases from 81.2% to 98.9% as the current density increases from 1 to 20 A g^{-1}, indicating excellent charge utilization.

Reference

[S1] S.K. Tiwari, S. Samuel, R.N. Singh, G. Poillerat, J.F. Koenig, P. Chartier, Int. J. Hydrogen Energy, 1995, **20**, 9-15.

[S2] S. Levine, A. L. Smith, Discuss. Faraday Soc., 1971, **52**, 290-301.

[S3] X. Feng, Y. Huang, C. Li, X. Chen, S. Zhou, X. Gao, C. Chen, Chem. Eng. J., 2019, **368**, 51-60.